RICE UNIVERSITY

Quantitative FLIM-FRET Measurement of Voltage Dependent Prestin Conformational Changes

by

Chance Mooney

A THESIS SUBMITTED

IN PARTIAL FULFILLMENT OF THE

REQUIREMENTS FOR THE DEGREE

Master's of Bioengineering

APPROVED, THESIS COMMITTEE

Robert M. Raphael, Chair
Associate Professor of Bioengineering

Michael Diehl
Assistant Professor of Bioengineering and Chemistry

Daniel M. Mittleman
Professor of Electrical and Computer Engineering

HOUSTON, TEXAS

January 2013

ABSTRACT

Quantitative FLIM-FRET Measurement of Voltage Dependent Prestin Conformational Changes

by

Chance Mooney

The transmembrane protein prestin forms an integral part of the mammalian sense of hearing by providing the driving force for the electromotility of the outer hair cell, a specialized cell that resides within the cochlea. This provides the cochlea with an ability to amplify mechanical vibrations, allowing for a high degree of sensitivity and selectivity in auditory transduction. The phenomenon, driven by changes in the transmembrane potential, is thought to be the result of conformational changes in self-associating prestin oligomers. We have previously utilized Forster resonance energy transfer (FRET), by both sensitized emission and acceptor photobleach methods, to detect prestin self -association. While these methods can qualitatively confirm prestin-prestin association, determining nanoscale changes in prestin organization requires greater accuracy than either technique provides. In this thesis, a FRET methodology based on fluorescence lifetime imaging (FLIM), detected by time correlated single photon counting (TCSPC), is implemented and utilized to quantitatively measure conformational changes within prestin-prestin oligomers in response to voltage stimulus.

Contents

List of Figures

List of Tables

Nomenclature

2PE	Two photon excitation
AP-FRET	Acceptor photobleach FRET
CFP	Cyan fluorescent protein
FLIM	Fluorescence lifetime imaging
FRET	Forster resonance energy transfer
HEK	Human embryonic kidney cell
IHC	Inner hair cell
IRF	Instrument Response Function
LSM	Laser scanning microscope
MCP-PMT	Micro-channel plate photomultiplier tube
NLC	Nonlinear capacitance
OHC	Outer hair cell
SE-FRET	Sensitized emission FRET
SHG	Second Harmonic Generation
SLC	Solute linked carrier
STAS	Sulfate transport anti-sigma factor
TAC	Time-to-amplitude converter
TCSPC	Time correlated single photon counting
TFP	Teal fluorescent protein
YFP	Yellow fluorescent protein

Chapter 1

Auditory Transduction

The phenomenon of auditory transduction in human beings involves some of the fastest and most complex biomechanics found in our physiology.

1.1. Mammalian Hearing

Mammals are able to transduce local pressure changes into sound via the operation of a specialized sensory system capable of both high sensitivity and dynamic range. The ear consists of several complicated substructures that work in a cooperative manner in order to achieve this goal. In general, sound waves are captured by the outer ear, channeled through the ear drum and compressed into the cohlea, then finally transduced into neural signals at the Organ of Corti.

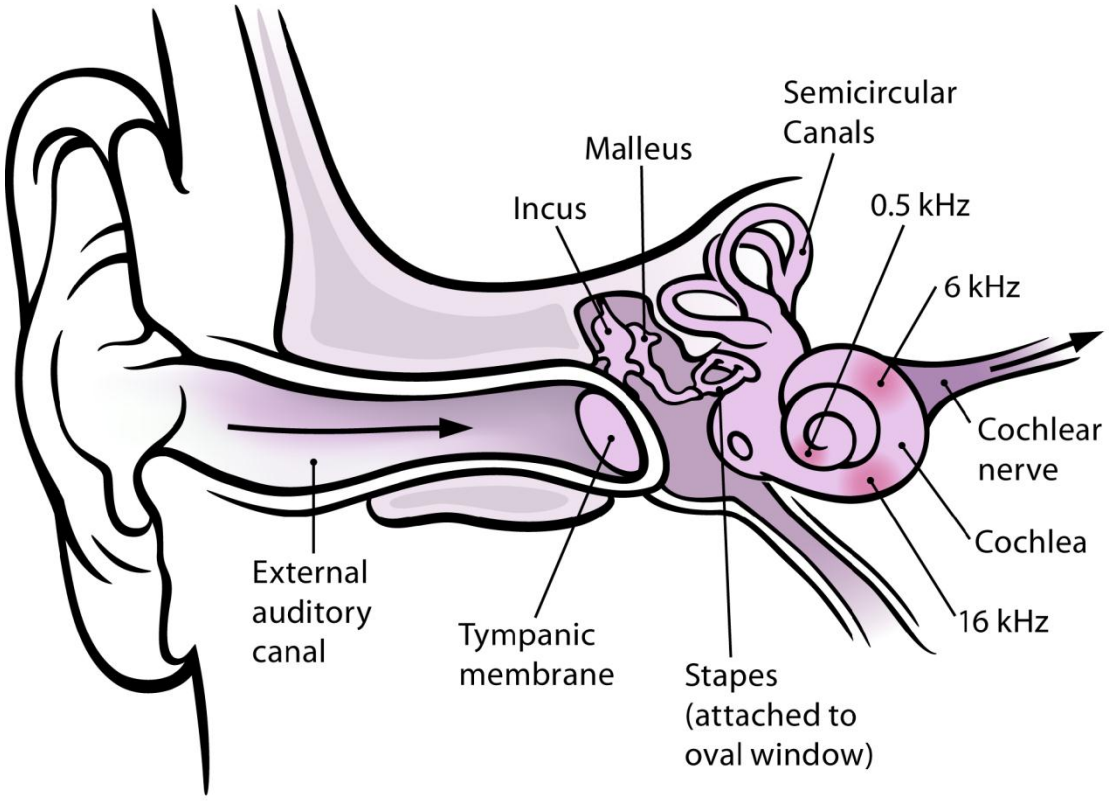

Figure 1.1 Overview of the human ear. Adapted from [1].

1.1.1. The Outer, Middle, and Inner Ear

The ear is divided into three sections that serve to concentrate sound waves. The outer ear includes the *pinna*, the visible part of the ear that provides a directional modulation to incoming sound, and the *external canal*, which channels sound into the *tympanic membrane*. This membrane transfers the sonic vibrations into the air-filled middle ear, containing the three ossicles: *malleus, incus,* and *stapes*. The middle ear transfers the vibrations of the eardrum to the fluid-filled inner ear, also known as the *cochlea*, via the ossicles, whose configuration provides a lever action that amplifies the wave pressure by a factor of 1.3. This coupling is made

between the tympanic membrane and the *oval window* of the cochlea. In addition, the oval window of the cochlea is much smaller than the tympanic membrane (17 times smaller), which further concentrates the pressure of sound waves for an overall pressure gain of 22-fold within the cochlear fluid [2]. This pressure gain is necessary in order to overcome the impedance mismatch between low-mass air and the relatively dense fluid of the cochlea. However, in the earliest example bioengineering, it was found that incident sound waves alone do not have the energy necessary to explain mammalian hearing sensitivity [3].

1.1.2. The Cochlea and The Organ of Corti

The cochlea is the site of transduction of mechanical vibrations into nerve signals to be transmitted to the brain, resulting in audio sensation. The cochlea itself is a multi-chambered spiraled tube, which hosts and supports the Organ of Corti (Figure 1.2).

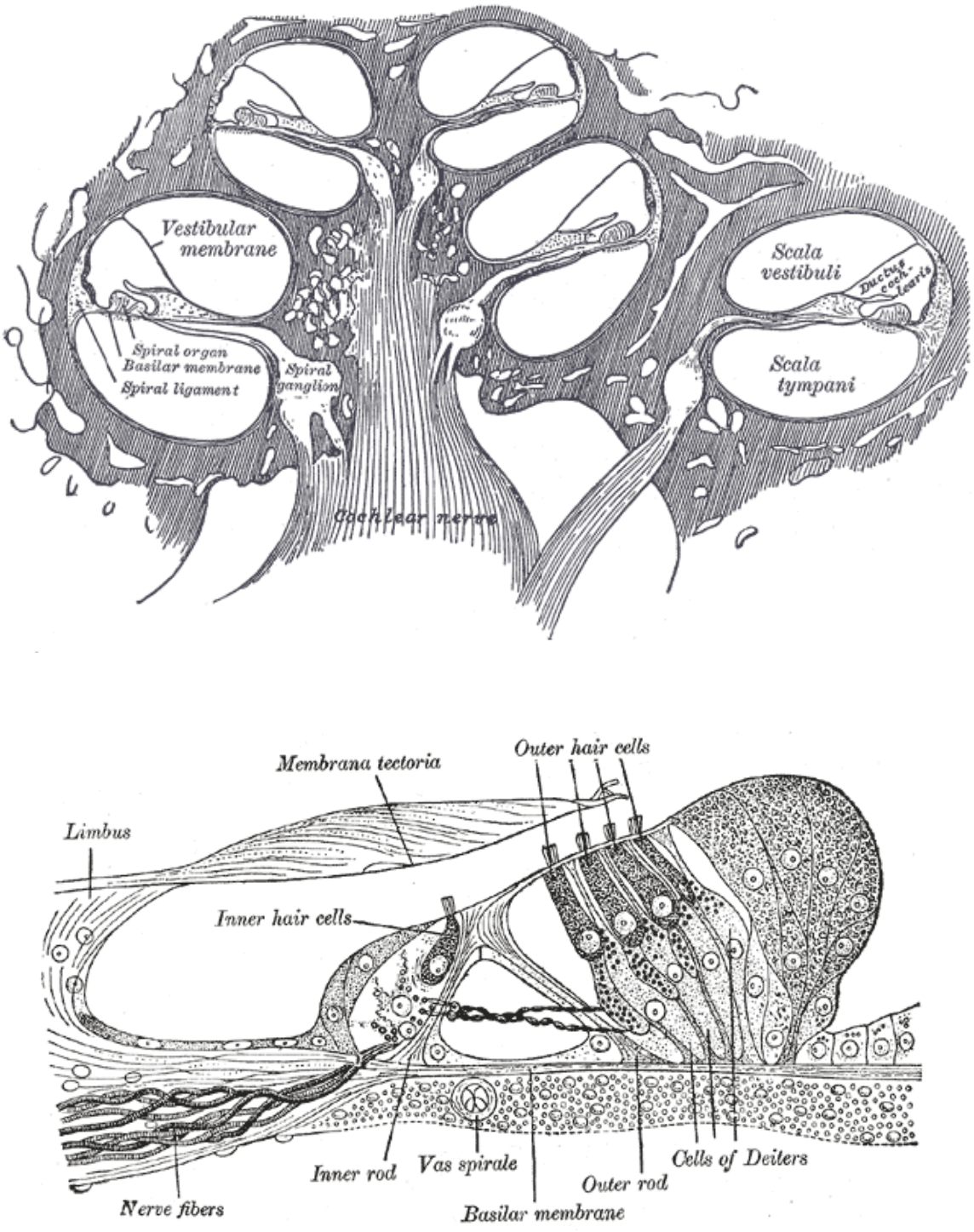

Figure 1.2 **Top:** Cross-section of the mammalian cochlea. **Bottom:** Cross-section of the Organ of Corti. Reproduced from [4]

The dense fluid of the cochlear duct reverberates with compression waves generated by the middle ear. Each section of the basilar membrane vibrates in response only to a narrow range of frequencies, with low frequencies activating near the base of the cochlea and high frequencies coupling with the apex of the cochlea [5]. As such, frequency selection in auditory transduction is based on cochlear depth. In effect, the cochlea acts as a biological Fourier transform, converting frequency to spatial coordinates.

The Organ of Corti is a specialized substructure that sits atop the basilar membrane of the cochlea, and is copied numerous times along the length of the cochlea. This organ is host to specialized sensory hair cells which are responsible for converting the motion of the basilar membrane into nerve impulses.

1.1.3. The Outer Hair Cells

Below the tectorial membrane of the Organ of Corti lie the inner and outer hair cells (IHCs and OHCs), which connect the cochlea to the brain. Tens of thousands of these elongated, tubular cells are arranged in rows along the length of the cochlea; one row consisting of IHCs, three rows consisting of OHCs. IHCs are flask-shaped cells that are surrounded in support cells and attached to afferent nerve cells. As illustrated in Figure 1.3 below, OHCs feature a cylindrical shape and are defined by three regions: the basal region connecting the cell to afferent and efferent nerve endings; the basolateral region that encompasses the lateral cylinder wall; and the apical region that includes the stereocilia 'hairs.'

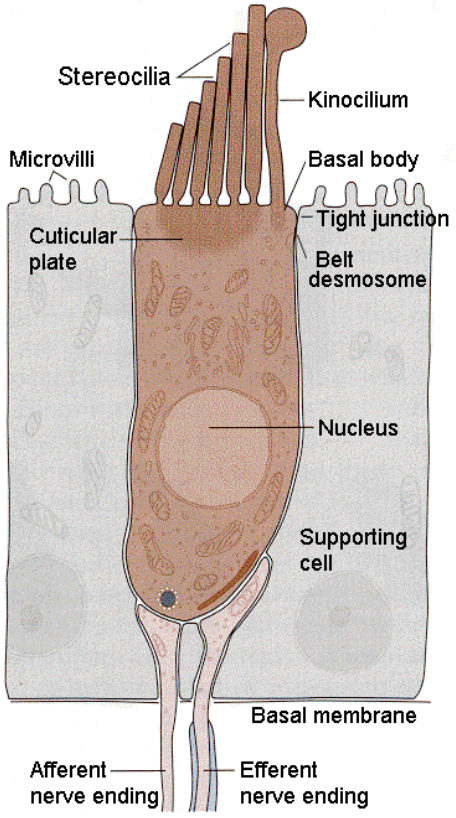

Figure 1.3 The outer hair cell. Reproduced from [6].

The apical region of each hair cell features an extended bundle of stereocilia, the 'hairs' of the hair cells, which connects to the tectorial membrane. Movement of the Organ of Corti against the tectorial membrane creates a shearing force on the cilia of the hair cells [7]. The resulting deflection of the hair cells opens ion channels within the cell membrane, causing the cells to depolarize in response to auditory stimulus. The inner hair cells react to this depolarization by generating action potentials that are transmitted to the brain via afferent nerves, but the outer hair cells display an altogether different response. OHCs react to depolarization and hyperpolarization by contracting and lengthening along their long axis, an

electromotile oscillation in response to auditory stimulus [8-10]. This action enables the OHCs to act as a biological active amplifier, injecting energy into the cochlea. The electromotility of the OHC has been found to be tightly coupled to charge displacement within the cellular membrane (Figure 1.4). Since this charge displacement is also a function of transmembrane voltage, it is a nonlinear capacitance (NLC) [11].

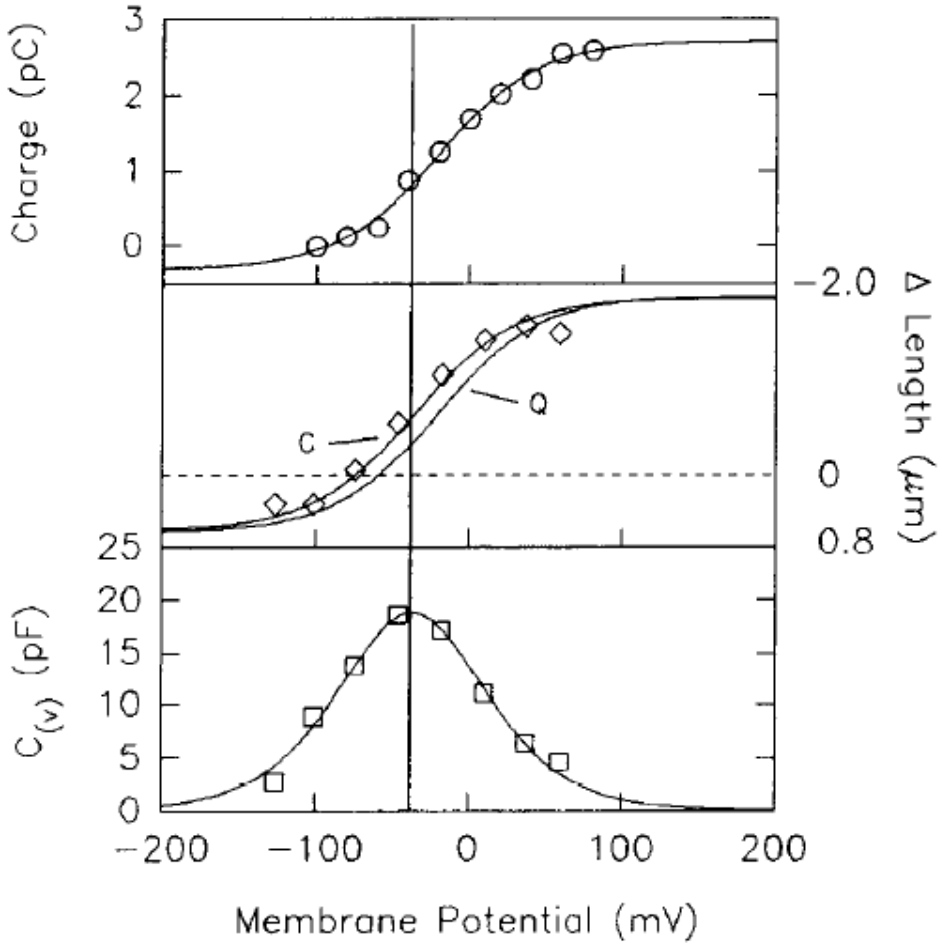

Figure 1.4 OHC behavior as a function of membrane potential. **Top:** Charge displacement. **Middle:** Length change. **Bottom:** NLC. The charge (Q) and capacitance (C) measurements are fit to the length changes of the OHC, demonstrating the strong electromotile coupling effect. Reproduced from [11]

1.2. Prestin

Discovered in 2000 by Dallos et al. [12] and named for the musical notation *presto* (fast), Prestin is the membrane protein that has been determined to be the 'prime mover' of the outer hair cell's electromotility, and therefore the basis of the Organ of Corti's auditory amplification [13, 14]. Comprised of 744 amino acids arranged into a 12-pass membrane protein, the exact topology of prestin is undetermined [15, 16]. The protein includes a STAS domain (sulfate transport anti-sigma factor antagonist) near the c-terminus. Fluorescent antibody tagging of prestin molecules reveals that it is localized in the lateral cell membrane of the OHC, but is absent from the apical or basal sections [17].

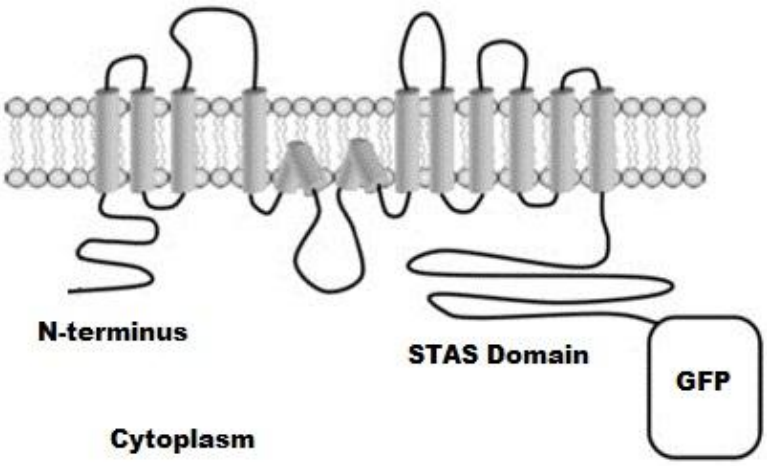

Figure 1.5 A hypothesized topology of prestin. The c-terminus that normally marks the end of a protein is the common attachment site for genetically encoded fluorescent proteins like GFP. Adapted from [18]

A member of a family of transporter proteins known as solute-linked carrier family 26 (SLC26) [19], prestin (SLC26A5) is an incomplete chloride anion membrane antiporter [20, 21]. (Unlike complete transporter proteins, prestin does not successfully release a bound anion during a cycle.) The SLC26 family has been found to be well conserved throughout the animal kingdom, from mammals to zebrafish to insects, while prestin itself is seen to be highly conserved in mammalian species [22, 23]. Transfection of the encoding gene for prestin into human embryonic kidney (HEK) cell cultures caused them to demonstrate voltage induced shape changes [12]. In addition, targeted deletion of the prestin gene in mice resulted in a loss of hearing ability without disturbing the OHC hairs [14].

1.2.1. Electrophysiology of Prestin

Prestin is known to produce a strong voltage-dependent NLC effect in both the native OHC as well as transfected human embryonic kidney cells (Figure 1.6Figure 1.6) [12]. It is well fit to a first derivative of a two-state Boltzmann distribution [11] often associated with ion transporters. This capacitance is a product of the movement of a charged particle within the prestin molecule across the plasma membrane, resulting in the generation of transmembrane potential. The correlation between the presence of NLC and electromotility in both native OHCs and transfected HEKs is further strengthened by salicylate treatment, a drug that is known to eliminate OHC motility as well as NLC in both OHCs and HEKs through competition with chloride anions [24]. The presence of prestin NLC within a

transfected cell is therefore commonly seen as a confirmation prestin function in model cells.

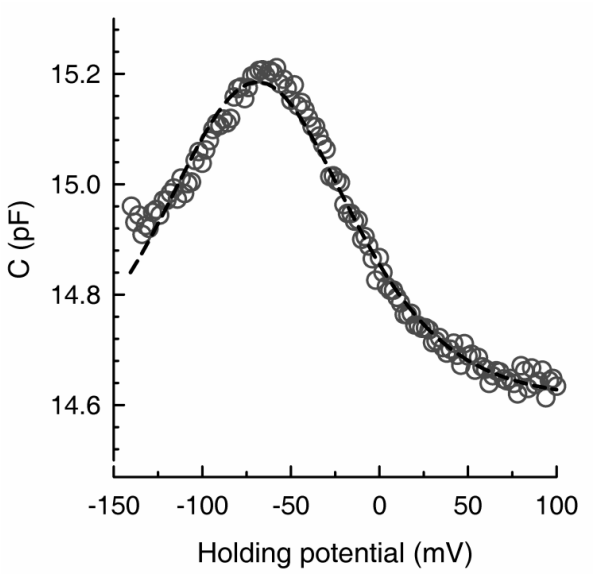

Figure 1.6 NLC trace of an HEK expressing prestin. The curve is fitted to the firs derivative of a two-state Boltzmann distribution function.

1.2.2. Prestin Self- Association

Prestin association with other proteins is known to occur in the OHC, as prestin containing particles in OHCs tend to be 8-10nm in diameter, sufficient for ~50 transmembrane domains [25]. This association is thought to be mediated through the STAS domain of prestin, an intracellular section of the protein that is common to all members of the SLC26 family. Though little is known about which proteins are able to interact with prestin or the larger role these interactions play in OHC motility, there is clear evidence of prestin-prestin interactions within transfected HEK model cells [26].

Though prestin is known to be a necessary component of electromotility, the direct action of the molecule has yet to be reported quantitatively. However, using fluorescently labeled prestin constructs, some information on prestin function has been elucidated. Using multiple Forster resonance energy transfer (FRET) methods, prestin has been observed to self-associate in HEK cells, with FRET efficiencies ranging from 5% to 30%. While sufficient to confirm self-association, this wide variance in reported FRET efficiencies prevents these methods from being used to detect relatively subtle conformational changes within the prestin molecule.

1.2.3. Membrane Motor Models

Owing to the high degree of conservation between prestin and the rest of the SLC26 family of membrane transporters, it is currently thought that the prestin motor functions through changes in conformational states. These conformational changes would mechanically interact with the cellular membrane to impart electromotility upon the larger host cell.

Two competing model of prestin-membrane mechanical action have been proposed, the membrane area motor model[27, 28] and the membrane bending model [29]. The area motor model hypothesizes that prestin functional groups change conformations such that the local membrane space is either expanded or contracted. Through the action of many prestin molecules, the OHC membrane as a whole is forced to lengthen or shorten.

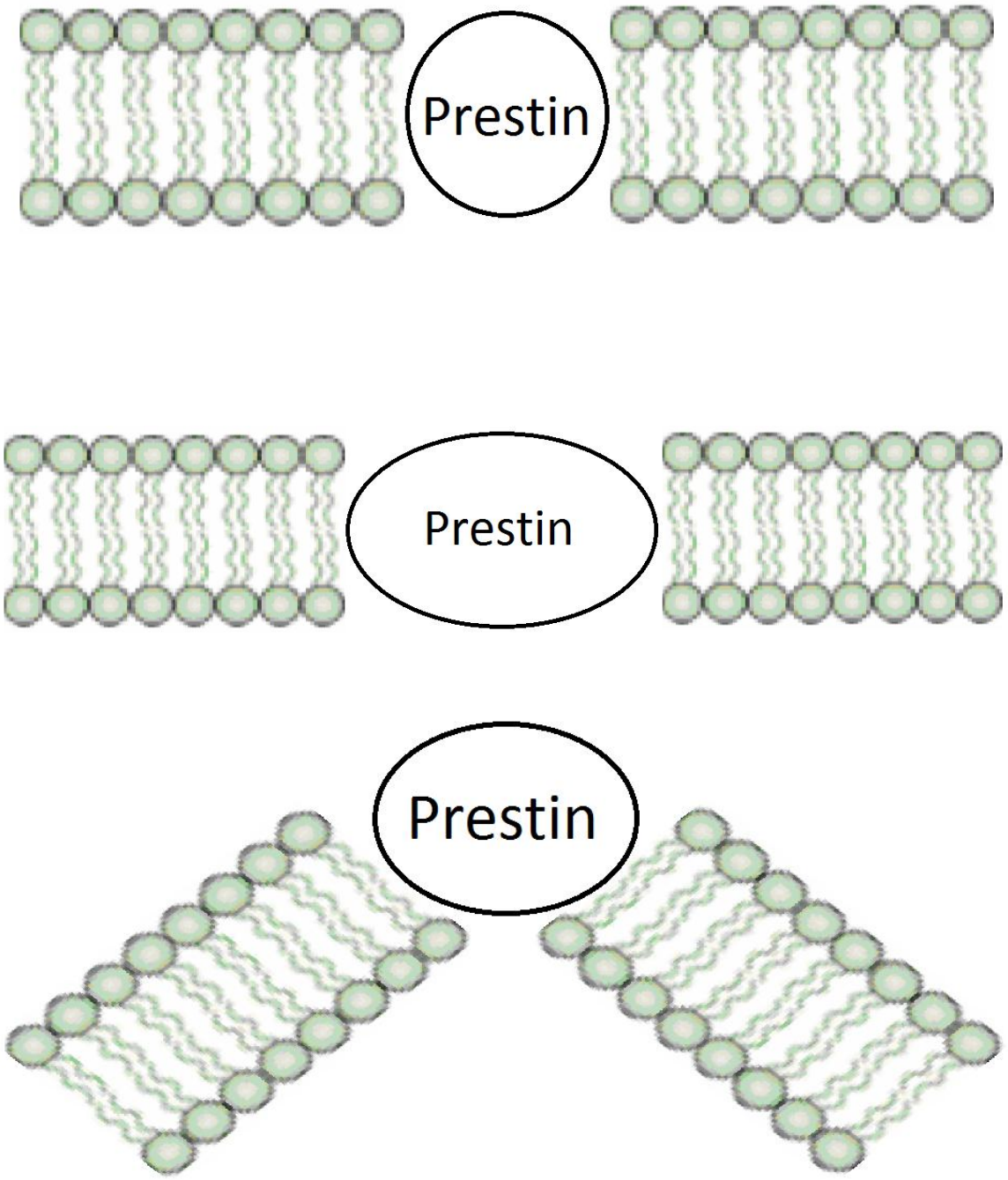

Figure 1.7. Models of prestin action on cell membranes. **Top:** Prestin in an inactive conformation. **Middle:** Membrane area model of prestin activity. **Bottom:** Membrane bending model of prestin activity.

In contrast, the bending model instead proposes that prestin conformational changes force curvature on the local membrane space. Through the action of all prestin throughout an OHC, the membrane is compressed into an accordion-like structure, shortening the cell overall. Both of these models assume that each prestin oligomer acts as a local area membrane motor. In order to confirm that prestin behaves according to either of these models, it is necessary to detect mechanical action on a nanometer scale.

Chapter 2

Fluorescence Techniques

In this section we review theory supporting the advanced optical microscopy techniques involved in this study of prestin.

2.1. Forster Resonance Energy Transfer

Forster resonance energy transfer (FRET) is a nanometer scale event that allows information to be extracted from biological systems beyond the diffraction limit of visible light. This phenomenon occurs when one fluorophore, the donor, nonradiatively transfers energy to a second fluorophore, the acceptor. The result is that an excited fluorophore is quenched, while a second fluorophore emits light without direct illumination. The probability that this event will occur is strongly dependent on the distance between the fluorophores and becomes vanishingly small at distances greater than a few nanometers. Using this property, the

occurrence of FRET in a sample provides evidence that two fluorophores, and therefore two sites of interest, are in close proximity.

Theodor Forster first described the resonance energy transfer process in 1948 with the following set of equations [30]:

$$k_T = k_D \left(\frac{R_0}{r}\right)^6 \tag{2.1}$$

$$R_0^6 = \frac{9000(\ln 10)\kappa^2 Q_D}{128 n^4 \pi^5 N_A} J(\lambda) \tag{2.2}$$

Here, k_T is the rate of energy transfer from donor to acceptor, k_D is the decay rate of the donor in the absence of an acceptor, r is the distance between donor and acceptor, and R_0 is the Forster radius. In Equation 2.2, Q_D, κ, $J(\lambda)$, n, and N_A, represent donor quantum yield, dipole orientation factor, spectral overlap integral between donor emission and acceptor absorption, index of refraction of the local medium, and Avogadro's number respectively. Most of the variables defining the Forster radius are physical properties inherent to the fluorophores involved and are static throughout the course of an experiment. The κ^2 dipole orientation factor is an exception, which can range in value from 0 to 4. A standard assumption for this variable is that it can assumed to be 2/3, the average value for two freely and rapidly rotating dipoles [31]. It should be noted that the above equations assume on a single donor acceptor pair are engaging in FRET activity, but in reality multiple acceptors can pair with a single donor.

The energy transfer efficiency *E*, the fraction of photons transferred to the acceptor fluorophore can be expressed as:

$$E = \frac{k_T}{k_D + k_T} = \frac{1}{1+(r/R_0)^6} \quad (2.3)$$

With typical values for the Forster radius being less than 10nm, FRET is commonly used to investigate protein-protein interactions, as the extremely short range of the phenomenon provides an optical measure of physical association [26, 32]. A typical, and highly convenient, setup for FRET study makes use of fluorescent proteins to study live cells. A frequently used donor-acceptor pair are the cyan and yellow fluorescent proteins, which possess a Forster radius of 5nm. These proteins can be genetically encoded into the DNA sequence for the protein being studied, introduced to a host cell, and produced by the cell's own physiology. This ensures that every protein of interest is labeled and avoids the difficulties often encountered in external labeling. While fluorescent proteins offer many conveniences and advantages over extrinsic labeling, there is one drawback: the large size of the protein itself. These fluorophores generally tend to have the chromophore of the molecule at the center of a large barrel structure, which has physical dimensions of 2.4 by 4.2nm (as seen in CFP and YFP) [33]. As such, the fluorophores themselves can occupy an appreciable amount of valid FRET distance with their own structure.

FRET efficiency can be measured by many methodologies, the most relevant of which are sensitized emission (SE-FRET), acceptor photobleach (AP-FRET), and

fluorescence lifetime imaging (FLIM-FRET) [34]. Each method has its own set of advantages and disadvantages.

2.1.1. FRET Methodologies

SE-FRET. Sensitized emission FRET directly detects energy transfer by exciting the donor fluorophore and measuring the acceptor emission. In theory, all acceptor emission would be due to FRET activity. This method requires a minimum of three controls for each measurement, as spectral crosstalk and background noise can be difficult to overcome in a quantitative fashion, but the technique is relatively easy to implement on standard fluorescence microscopes and can be applied across a wide field image with few limitations.

AP-FRET. Acceptor photobleach FRET approaches energy transfer in reverse through the perspective of donor quenching. As successful FRET interactions prevent donor emission, the efficiency of energy transfer can be determined from the loss of donor fluorescence in FRET systems. This is measured by bleaching the acceptors in a small region and monitoring the recovery of donor intensity as the source of the quenching effect is destroyed. This technique is more applicable to quantitative study of FRET efficiency than SE-FRET and is relatively easy to implement, but spectral crosstalk remains an issue.

FLIM-FRET. In fluorescent lifetime imaging FRET, the interaction between fluorophores is measured by a decrease in the characteristic lifetime of the donor fluorescence when interacting with an acceptor. This detection scheme is

completely independent of the acceptor and is less influenced by intensity, allowing for the most reliable measure. Unlike other FRET methods, FLIM-FRET relies on specialized instrumentation, limiting its availability. Additionally, data analysis can be more burdensome, requiring longer exposure times than other methods. FLIM-FRET is the method of choice for this work and will be discussed in greater detail.

2.1.2. FRET Precision

To date, FRET has been mainly and most easily used as a binary indicator of activity, where two fluorophores can be seen to be in proximity to each other [26]. Quantifying the relatively small changes in efficiency that accompanies small movements within the Forster radius can be difficult when using SE- and AP-FRET. Both background noise and cross-talk between narrow spectral channels can be on the same order of magnitude as the changes in intensity that are being sought. Intensity based FRET measurements are also unable to distinguish between intensity changes caused by actual FRET activity and changes in the FRET participation rate of a population [31]. Finally, the intensity of a measurement depends on external parameters such as excitation intensity and probe concentration.

As FLIM-FRET measures the donor fluorophore's lifetime, it largely avoids spectral cross-talk and noise and can easily separate changes in FRET efficiency and participation rate. It is quickly becoming the preferred technique for quantitative experimentation. In a study on chromatin packing during mitosis, Lamond et. al.

detected four distinct packing states of chromatin with a FRET efficiency range of 0%-9% [35]. Meanwhile Beltram et. al. compared FLIM-FRET and AP-FRET techniques with a model system, finding that FLIM-FRET was 6-fold more precise in the measurement of efficiency [36]. Utilizing this new technology is the ideal path for assessing conformational changes in prestin via FRET.

2.2. Fluorescence Lifetime Imaging Microscopy

The methods and theories of fluorescence spectroscopy in the spectral domain are well known and have seen extensive use throughout the sciences for centuries. When any chromophore absorbs energy and is excited, it enters into a high energy state of some form. This high energy state then has a constant non-zero probability to spontaneously revert to a lower energy state at any time, releasing energy in the process. The average length of time that the fluorophore spends in this excited state is known as its fluorescence lifetime [31].

The fluorescence lifetime of a fluorophore is an environmentally sensitive parameter, and is in general affected by quenching effects in the local area. By observing the lifetime of a sample, we can have access to a wealth of information all while remaining intensity independent. FLIM is therefore a robust imaging methodology, insensitive to variations in excitation power, fluorophore concentration, photobleaching, and many other parameters that can negatively impact traditional spectral microscopy.

While there are multiple instrumentation schemes capable of detecting fluorescence lifetimes [31], the method used for this work is time correlated single photon counting (TCSPC). By measuring the time between photon absorption and emission through the use of pulsed light sources, synchronized fast electronics, and ultrafast photon detectors, a great deal of useful information can be extracted.

2.2.1. Fluorescence Lifetime

The fluorescence lifetime of a fluorophore is determined by the internal decay rates of its photophysical structure [31]. A population of excited state molecules n_0 will therefore decay at a constant rate of k over time according to:

$$\frac{d}{dt}n(t) = -k\,n(t) \tag{2.4}$$

This is easily solved with:

$$n(t) = n_0 e^{-k\,t} \tag{2.5}$$

Now since fluorescence intensity is proportional to the excited state population and defining $\tau = k^{-1}$:

$$I(t) = I_0 e^{-t/\tau} \tag{2.6}$$

In reality, a fluorophore may in fact have several separate fluorescent decay pathways, each with an independent decay rate of k_i. Equation 2.6 above is then in fact the single decay special case of a more general intensity decay:

$$I(t) = \sum_i a_i e^{-t/\tau_i} \tag{2.6}$$

2.2.2. Time Correlated Single Photon Counting

A detection scheme made practical by the confluence of ultrafast light sources, electronics, and single photon detectors, a TCSPC system is able to record the time-of-arrival of a photon with picosecond accuracies [31]. TCSPC systems, and the high accuracy equipment involved, allow the implementation of powerful microscopy techniques such as FLIM by directly measuring the time delay between individual absorbance and emission events.

The principle behind a TCSPC measurement is the use of a time-to-amplitude converter (TAC) as a timer. This timer is started by a pulsed light source that is simultaneously used to excite a sample. The TAC then starts a voltage ramp that is linear with respect to time. The TAC is stopped upon detection of an emitted photon, whereupon the TAC voltage is processed through an analog-to-digital converter. An individual count is then added to the appropriate time channel in a histogram. By repeating this measurement many times over and collecting the arrival times of the photons into a histogram, a fluorescence decay profile can be

built as in Figure 2.2. Using nonlinear least square curve fitting, the fluorescence lifetimes can then be extracted.

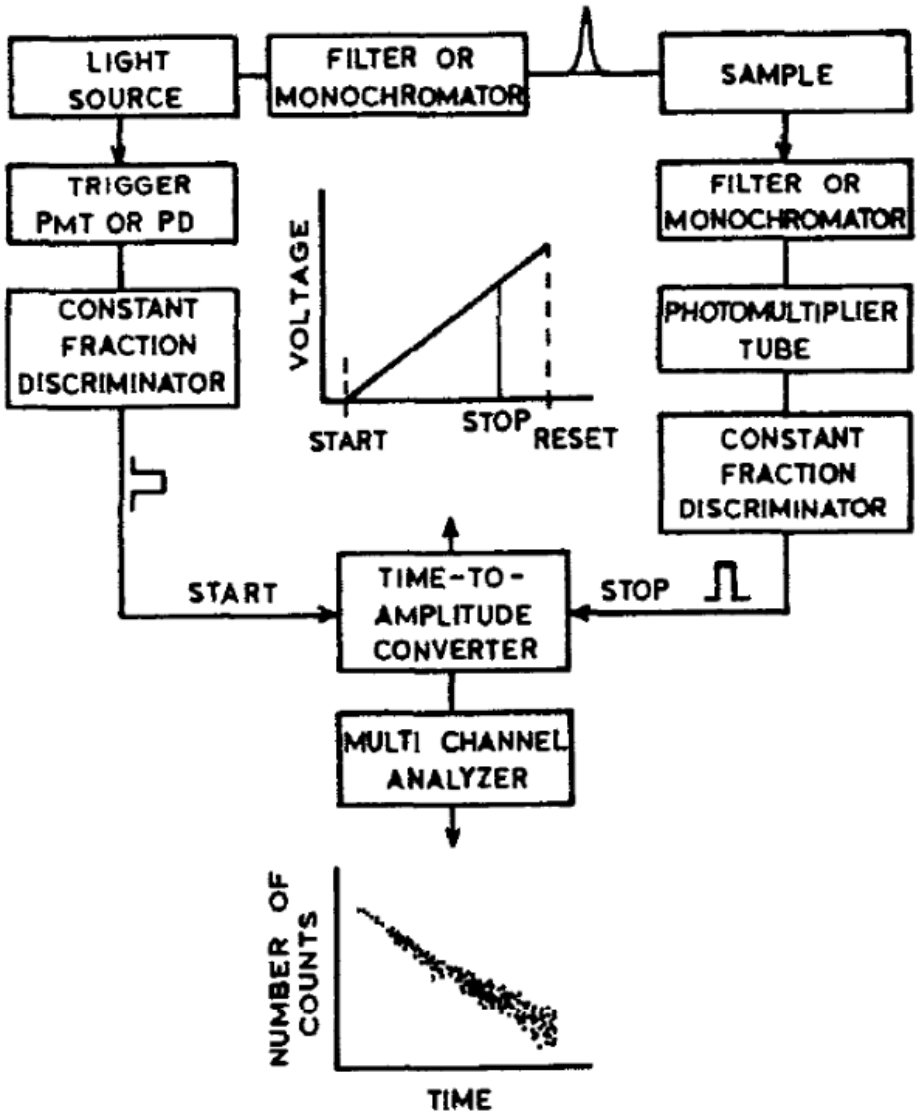

Figure 2.1 Schematic for time-correlated single-photon counting. Reproduced from [31].

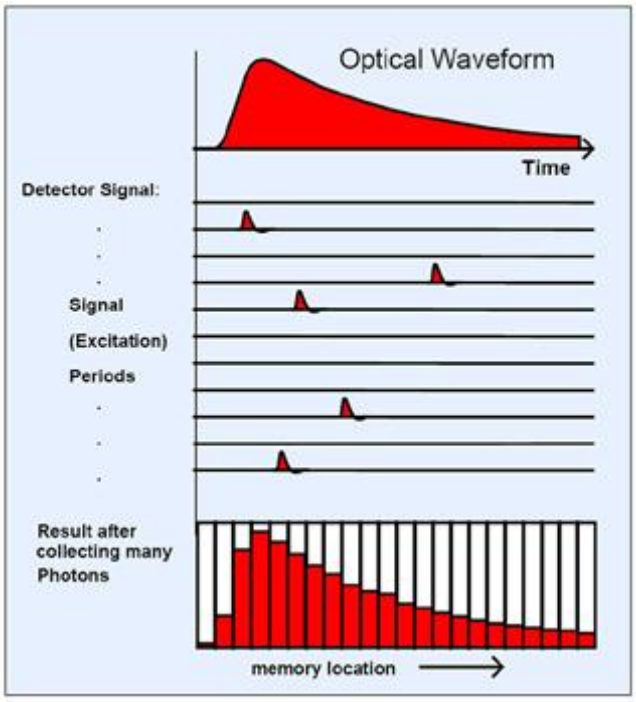

Figure 2.2 Many repetitions of the basic TCSPC experiment builds an approximation of the time course of fluorescence. Adapted from [37].

2.2.3. FLIM-FRET

The intensity-independent FLIM approach to measuring FRET efficiencies has many advantages over the older techniques of SE-FRET and AP-FRET. By measuring only the lifetime decay of the donor fluorophore, common sources of error in FRET measurements, such as fluorescence crosstalk and FRET population participation are eliminated. Additionally, the technique provides its own control measurement in the same exposure as the experiment itself.

From the perspective of the donor fluorophore, the effect of a FRET system is to provide the donor fluorophore with a new relaxation pathway. Fortunately, in a

FRET system this new decay constant is already defined by Equation 2.1. This new decay pathway directly competes with the native decay pathway, depressing the original lifetime of the donor as in Figure 2.3. This results in a new fluorescence lifetime τ_{DA} (Figure 2.3) for the molecule. For molecules that display multi-exponential decay profiles, each lifetime is reduced by FRET competition.

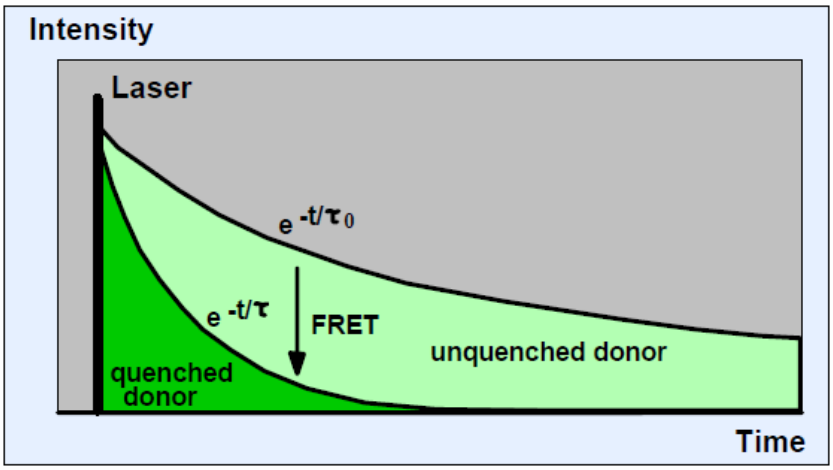

Figure 2.3. FRET induced changes in the native fluorescence lifetime τ_0 leads to a reduced lifetime τ. Reproduced from [37]**.**

In each population that is measured, there will be both interacting and non-interacting subspecies of the donor. Non-interacting donor fluorophores will display the ordinary donor lifetime, τ_D. The overall measurement will therefore capture both τ_{DA} and τ_D, resulting in a multi-exponential decay profile. FRET efficiency can then be calculated by:

$$E = 1 - \frac{\tau_{DA}}{\tau_D} \tag{2.7}$$

2.2.1. Two Photon Excitation and Second Harmonic Generation

TCSPC requires the use of a pulsed light source in order to provide a definite time of excitation, but there are many choices that can fulfill this requirement. The use of a femtosecond pulse laser as the light source enables us to take advantage of an optical technique called two-photon excitation (2PE). By focusing the photons generated by the laser in both time (pulsing) and space (optics), an extremely high photon flux can be achieved in a femtoliter volume of space. This in turn allows a fluorophore the possibility of absorbing two low energy photons near simultaneously, combining their energies into a single excited state that can decay as normal [38]. There are several advantages to this approach, such as increased imaging depth in tissues and excitation of only the focal spot.

A non-linear optical effect, second harmonic generation (SHG) is similar to 2PE, as both absorb two photons at nearly the same instant. Unlike 2PE, where this energy is used to raise a fluorophore to an excited state, SHG directly emits a single photon of twice the original energy [39]. Both phenomenon require a very high photon flux; however, SHG is generated only from select materials. Collagen, a common extracellular matrix protein found in many tissues as well as most *in vitro* cell culture such as HEKs, is a known source of SHG [40]. While SHG can be used as an imaging technique, in FLIM it is a source of time-dependent noise.

Chapter 3

Methodology

This section provides details on the specific techniques involved in this thesis that are common to the experiments performed.

3.1. System Configuration

The complete TCSPC system consists of the following critical components: a Zeiss LSM510 laser scanning microscope, a Coherent Chameleon ultrafast laser, one Becker & Hickl SPC-150 TCSPC board, and a Hamamatsu R3809U-52 MCP-PMT. The LSM510 serves as the base of the system, providing automated imaging capabilities via raster scanning. The system is assembled in the configuration seen in Figure 3.1.

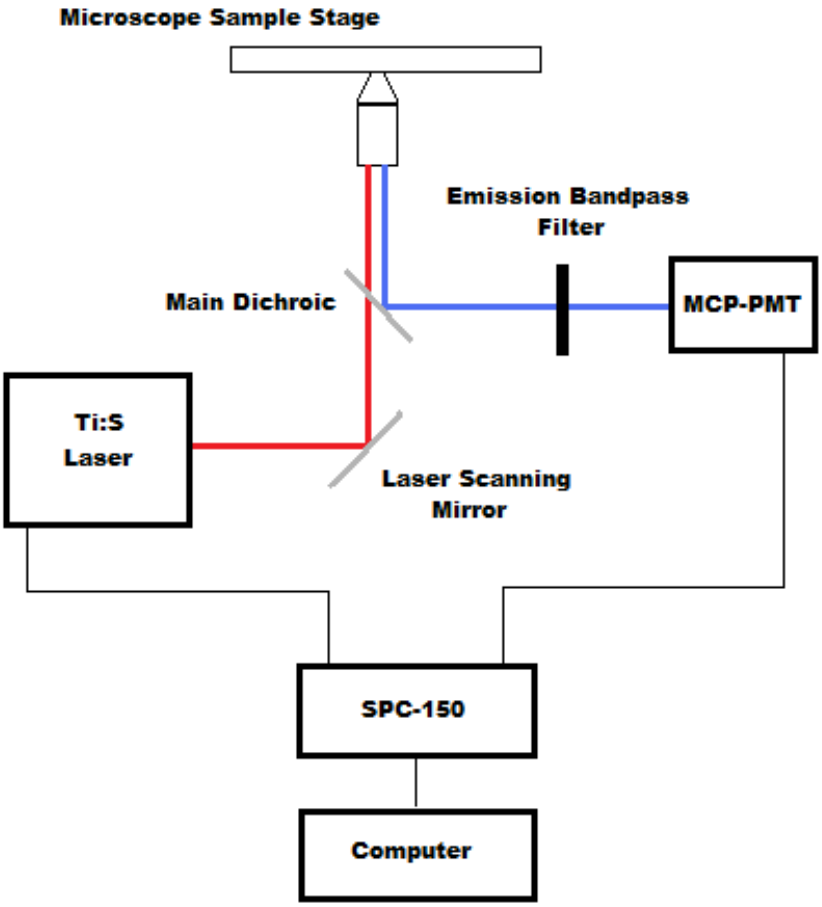

Figure 3.1 Schematic of FLIM system.

The Coherent Chameleon ultrafast pulsed laser, a Titanium:Saphirre laser operating on the Kerr-Lens mode locking principle, possesses a 90 MHz repetition rate with a pulse width of approximately 120 femtoseconds. These properties simultaneously allow a pulse of excitation light to be well located in time and provides a two-photon excitation source. The timing information of these pulses are relayed electrically to the TCSPC board through a synchronization signal generated by a photodiode integrated into the Chameleon laser housing. While ultrafast

pulsing is beyond the requirements of TCSPC, the Chameleon laser allows us to implement two-photon excitation of samples.

A Becker & Hickl SPC-150 TCSPC board hosts the TAC and ADC used to process signals received from the Chameleon laser and Hamamatsu MCP-PMT. This board allows for a single detection channel with a maximum time resolution of 716 femtoseconds. It is hosted in a standard x86 Microsoft Windows based PC and operated with Becker & Hickl software. It is capable of automated raster image collection through the use of external clock signals provided by the Zeiss LSM510.

Accurate timing information for detected emission photons is provided by a Hamamatsu R3809U-52 micro-channel plate photomultiplier tube (MCP-PMT) that delivers a time resolution of 22 picoseconds and a detection window of 400nm to 650nm. It will be mounted in the non-descanned detection path in order to provide greater photon collection efficiency. The instrument response function (IRF) of the detector was measured through second harmonic generation in potassium dihydrogen phosphate crystals.

An HFT KP 650 (Zeiss) main dichroic beam splitter was used as the excitation filter. Long wavelength laser light is allowed to pass through this dichroic into the sample. Subsequent two-photon excitation of the sample releases short wavelength emission photons that are deflected by the dichroic into the non-descanned beam path for detection by the MCP-PMT, after being filtered through a custom ET495/30 bandwidth filter (Chroma, Bellow Falls, Vermont).

3.1.1. Reverse Start-Stop TAC Operation

The TCSPC system, as mentioned above, measures time using a linearly charging capacitor circuit. It should be noted that the SPC-150 board operates in a "reverse start-stop" configuration, where instead of measuring the time from excitation pulse to emission detection, the TAC is started when an emission photon arrives. The TAC then continues to run until the next synchronization signal is received from the next excitation pulse. If the period of the excitation pulses is known and constant, then the time elapsed between the previous excitation and emission can be easily found. The Chameleon laser satisfies this requirement with a constant pulse rate of 90 MHz and a pulse jitter smaller than 20 femtoseconds.

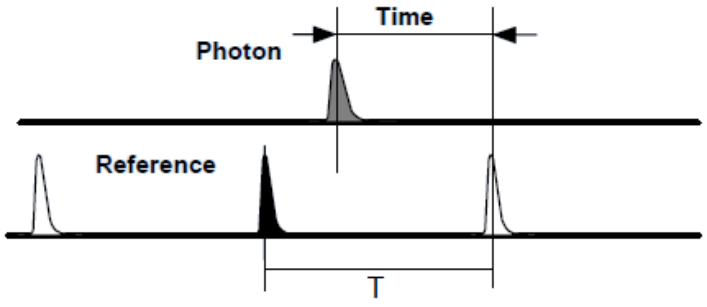

Figure 3.2. Reverse start stop pulse sequence. Modified from [37].

3.2. HEK Cell Preparation

Human embryonic kidney (HEK) cells have been commonly used to host fluorescent Prestin constructs in past experiments as the native OHCs are not

culturable and are only available through animal model harvesting [12, 18, 26]. Here HEKs are again used as the host for prestin experimentation. Adherent cell cultures provided by the Pereira laboratory of Baylor University were grown and maintained in T-75 flasks at 37 °C and in a 5% CO_2 atmosphere. The HEK culture is provided nutrients with Dulbelcco's Modified Essential Media (Lonza, Basel, Switzerland), containing 10% fetal calf serum and 1% PenStrep.

For transfection, 6-well plates were plated with HEKs from primary culture and allowed to grow to 50%-70% confluence. Using the commercial transfection reagent TransIT-LT1 (Mirus Bio LLC, Madison), HEKs were transiently transfected with prestin constructs. Mixtures consisting of 250 µL serum-free media, 7.5 µL LT1 reagent, and 2.5 µg of the appropriate plasmid DNA were added to each plate. For co-transfections, mixtures consisted of double the above volumes with 2.5 µg of each plasmid. 8 to 24 hours after transfection, cell cultures are replated using 0.05% trypsin at room temperature on to 22mm square No.1 glass cover slips at 3% confluence. 16 hours after replating, the glass cover slips are mounted in an open air chamber on the Zeiss LSM510 for imaging.

3.3. FLIM Measurement Protocol

Cells are imaged on the Zeiss LSM510 using a 63x 1.4 NA oil immersion objective. Individual cover slips are visually scanned for prestin expressing HEKs using a mercury arc lamp as a wide-field fluorescence source. Brightly fluorescent cells with membrane localized intensity profiles are then scanned using continuous

wavelength lasers and Zeiss PMTs to confirm adequate fluorescence and prestin localization for FLIM experiments. TFP and CFP are imaged using a 488nm argon laser (Zeiss), while YFP is excited with 514nm laser light. The region of interest (ROI) function of the LSM510 is then used to select only the clear and isolated sections of cellular membrane, as seen in Figure 3.3. The LSM510 is then reconfigured to the setup described in section 3.1 above.

At this point, the room containing the microscope is blacked out and all personnel move outside; for the rest of the experiment the system will be operated remotely. The ROIs previously selected are then scanned with the Chameleon laser tuned to 867nm at 20% transmission and FLIM data is collected is collected over an exposure of up to fifteen minutes. The SPC-150 is configured to record the decay times of emitted photons in a histogram with 4096 time channels at 2.44 picoseconds per channel. During the course of the measurement, photon collection may be temporarily interrupted in order to compensate for stage or cell drift by realigning the ROIs.

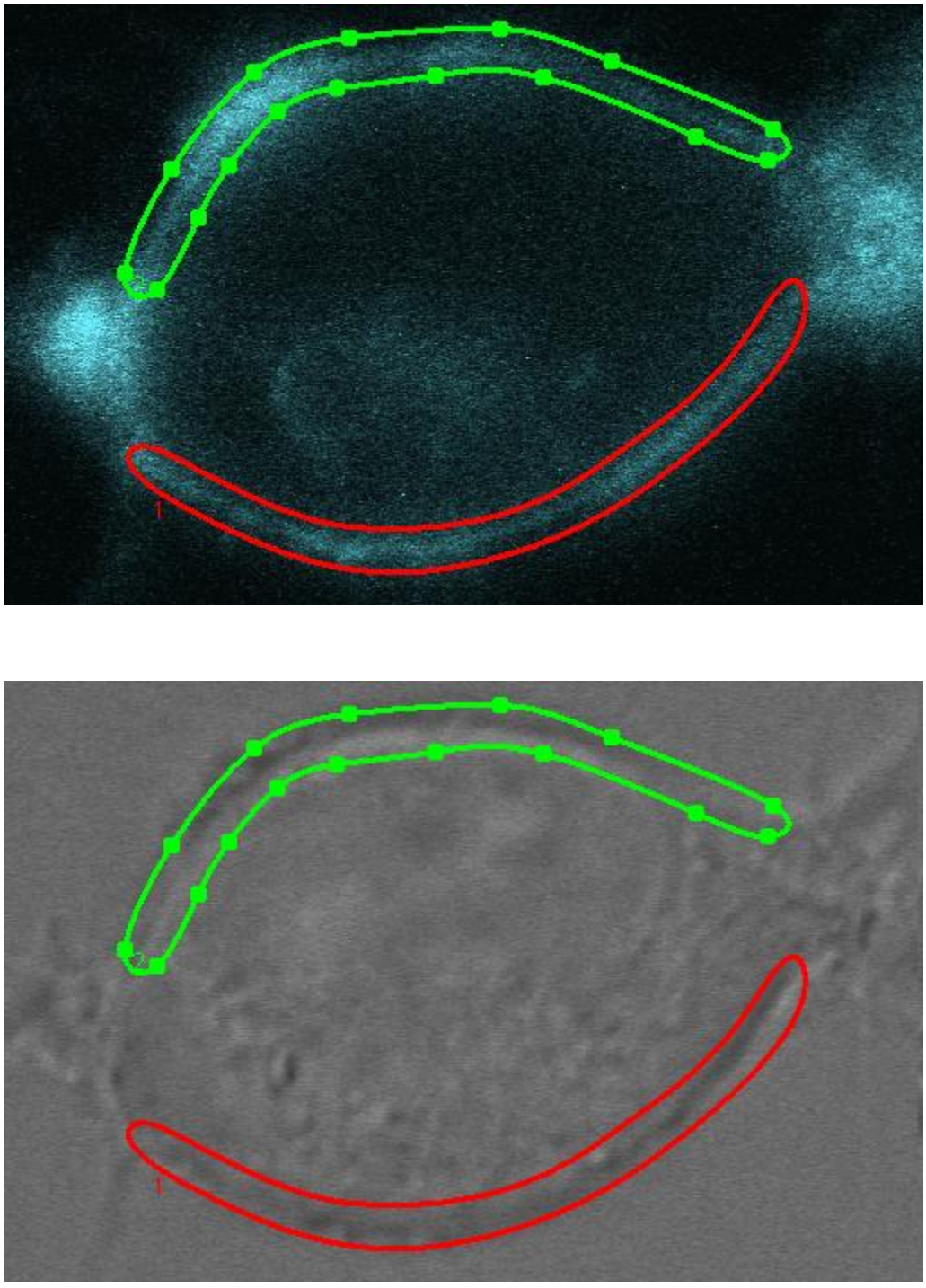

Figure 3.3 Typical HEK cell for FLIM recording. **Top:** Prestin-TFP fluorescence in HEK membrane. **Bottom:** Brightfield image of same cell. Only the areas inside the green and red sections will be scanned by the Zeiss LSM510 system.

3.4. Whole-Cell Patch Clamp

A central electrophysiological experimental apparatus is the patch-clamp. Using whole-cell patch-clamp methods, the electrical state of individual cells can be probed or altered as required. This experimental procedure is descended from the work of Hodgkin and Huxley on the giant squid axon in the 1950s [41]. The large diameter of the squid's axon (~1mm) allowed electrodes to be placed directly inside the length of the cell, along with externally attached electrodes along the length. This system was the first to directly record the propagation of action potentials within a neuron and resulted in the simplified electrical circuit model of a cell.

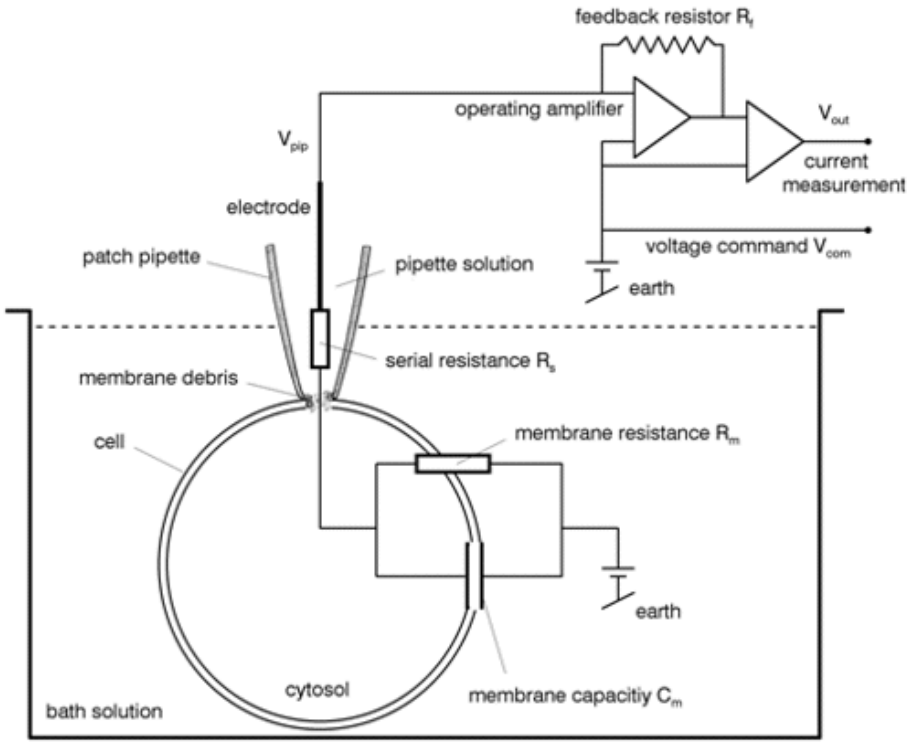

Figure 3.4. Electrical diagram of whole cell patch clamp. Reproduced from [42]

Current electrophysiology experiments, conducted on cells far smaller than the giant squid axon, are based on the system developed by Neher and Sakmann in 1976 [43]. In this system, electrical access to the cell interior is made through the use of a glass micropipette placed directly on the cell. This micropipette, having been forged with an opening at the tip only a few microns wide, contains an chlorided silver wire as an electrode and is filled with a buffer solution intended to replicate cytoplasmic ion concentrations. The micropipette is pressed closely to the cell and a suction force is applied, forming a tight seal against the membrane. Then the suction force is used again to breach the cell membrane at the contact point, providing a continuous solution between electrode and cell interior. At this point, electrical access to the cell is achieved, and an attached amplifier can be used to record signals in response to various stimuli or to hold, or "clamp," the current or voltage of the cell to a desired value (referenced to a bath electrode).

Patch pipettes were pulled from borosilicate capillary tubes 0.8-1.1 x 100mm (Kimble Chase) using a Sutter Instruments P-97 pipette puller. The electrophysiology was performed using an EPC10 plus amplifier (HEKA, Mahone Bay, Canada). The use of ionic blocking solutions permits the analysis of the capacitive current in isolation from voltage dependent ionic conductance. Glass pipettes with resistances between 2.5 to 3.5 MΩ were filled with a blocking solution containing 130 mM CsCl, 2 mM MgCl2,10 mM EGTA and 10 mM HEPES. The bath blocking solution contains 99 mM NaCl, 20 mM TEA- Cl, 2 mM CoCl2, 1.47 mM MgCl2 ,1 mM CaCl2 ,10 mM HEPES. These solutions are both titrated to pH 7.2 and

320mOsm (Osmette A, Precision Systems, Natick, MA). To determine the membrane capacitance of HEKs, we used a phase-sensitive detector implemented in PatchMaster software (HEKA). An 800-Hz, 10-mV sine wave is applied to patched isolated, patched cells while the current response is measured as DC holding potential was stepped from -100 to +100 mV in 2 mV increments. At each DC potential, four complete sinusoidal voltage cycles occurred, and discrete capacitance values were automatically calculated from the last three. Only cells that showed typical prestin NLC curves were assayed with FLIM for voltage-clamped FRET measurements.

3.5. Lifetime Decay Analysis

Lifetime decay constants are generally estimated through least squares fitting curve fitting of the recorded TCSPC histogram, but the test function to be used is not a simple fluorescence decay [31]. While Equation 2.6 describes ideal case, it has several underlying assumptions: both excitation and detection are δ-functions with no timing inaccuracies, and no time-independent background noise or time-dependent SHG noise. In real systems, both excitation and detection have limited time accuracy, as the pulse of the Chameleon laser and the R3809 response have finite widths.

These systematic errors, as well as noise, can be accounted for with a modified model function:

$$I(t) = IRF(t) \otimes \sum_i^n a_i e^{-t/\tau_i} + c + s * IRF(t) \quad (3.1)$$

Here, the lifetime decay function is convolved with *IRF(t)*, the experimentally recorded instrument response function. Fitting parameters *s* and *c* account for SHG noise and constant background noise respectively.

With the measured fluorescence trace *D(t)* actually being the convolution of the IRF and the desired decay components, curve fitting in TCSPC is typically performed using iterative reconvolution, where each iteration of the least squares algorithm convolves the test function with the IRF to generate the fitting function *F(t)*. The goodness of fit is measured with χ^2 parameter [44]:

$$\chi^2 = \sum_t^n \frac{[D(t)-F(t)]^2}{[\sigma(t)]^2} = \sum_t^n \frac{[D(t)-F(t)]^2}{F(t)} = \sum_t^n [W(t)]^2 \quad (3.2)$$

Due to the Poissonian statistics of photon counting, the expected deviation *σ(t)* at time *t* can be estimated as the square root of the number of counts at time *t*. The χ^2 statistic can normalized by the degrees of freedom, the number of data points *N* less the number of fitted parameters *p*:

$$\chi_r^2 = \frac{\chi^2}{N-p} \quad (3.3)$$

For a good fit χ_r^2 should be close to one. A second useful judge of fitting quality are the weighted residuals *W(t)*, which in a good fit should be randomly distributed about zero. χ_r^2 values greater than 1.2 or structure in the residuals are an indications of poor fits. In this work, SPCImage from Becker & Hickl provides the nonlinear least squares iterative reconvolution algorithm used for all curve fitting. In each curve fit, at least 3600 time channels of the TCSPC histogram are used for lifetime estimation.

Chapter 4

Voltage Dependent FLIM-FRET

Using fluorescence lifetime imaging methods to monitor Forster resonance energy transfer, we have the ability to monitor the conformational changes within individual prestin oligomers. This work demonstrates a quantitative measure of these changes, beyond the qualitative detection schemes offered by older methodologies by replacing the older systems involved in previous measurements with more statistically reliable substitutes. All patch-clamp experiments were completed with the assistance of Guillaume Duret from the Raphael lab.

4.1. FLIM-FRET using CFP-YFP

Previous investigations of prestin mechanics via FRET made use of the classic donor-acceptor pair cyan fluorescent protein and yellow fluorescent protein (CFP and YFP). Prestin constructs containing these fluorophores were used for the

previous studies of nanoscale interaction via SE-FRET and AP-FRET methodologies; as such, the CFP-YFP pair is a natural first choice for FLIM-FRET. In order to establish the newly implemented Becker & Hickl TCSPC system as reliable, we chose to replicate previously obtained data from wild type prestin as well as two mutated prestin variants (D645E and N548Q), provided by Lavanya Rajagopalan of Baylor University. For this unpatched control experiment, the cotransfection consisted of wild type prestin-YFP and either D645E, N548Q, or wild type prestin, each carrying a CFP tag on the c-terminus as usual. CFP-YFP FLIM-FRET lifetime traces are fit to a 3τ model; only fits with χ^2_r <1.2 are accepted. Figure 4.1 compares the results of the AP-FRET and FLIM-FRET systems.

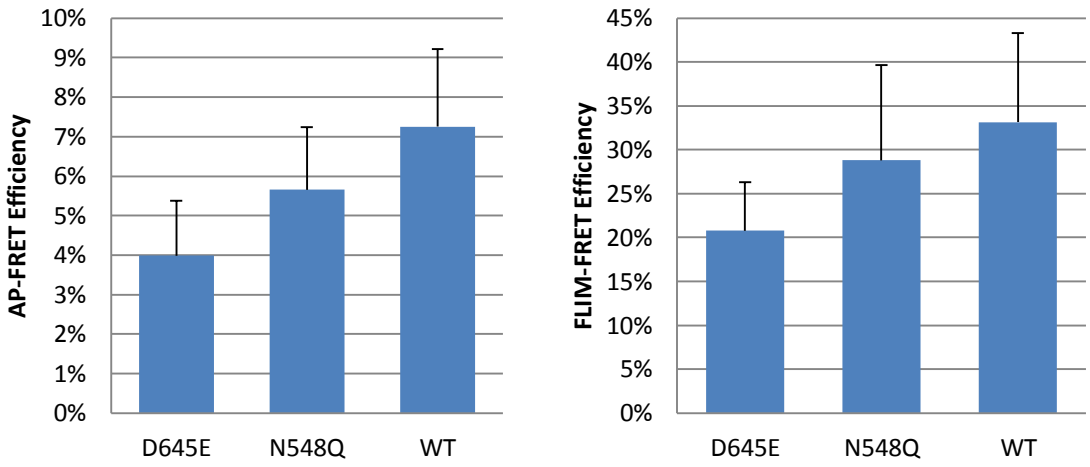

Figure 4.1 FRET efficiencies *E* of mutant or wildtype prestin-CFP and prestin-YFP. **Left:** AP-FRET methods. WT: *E*=7.2%±1.9% N548Q: *E*=5.7%±1.6% D645E: *E*=4.0%±1.4% **Right:** FLIM-FRET methods. WT: *E*=33%±13% N548Q: *E*=29%±15% D645E: *E*=21%±7.9% All errors are standard deviations. n=6 or better for each measurement.

In general, both FLIM-FRET and AP-FRET come to similar results on relative FRET efficiencies. While FLIM-FRET methods did show a much higher absolute FRET efficiency, both mutant variants of prestin displayed lower efficiency than wild type, with D645E significantly so ($p<0.1$ according to Students *t*-test). Consistent results between measurement the methodologies demonstrate that the FLIM-FRET system implemented in the Raphael Lab functions appropriately, but a cursory examination of the standard deviations of the FLIM-FRET results indicate that the accuracy gains promised by TCSPC techniques have not been realized. We therefore found that the replacement of the CFP donor was necessary in order to achieve higher sensitivity in FRET measurement.

Cyan fluorescent protein is well known to possess a natural bi-exponential lifetime decay profile. When introduced into a FRET system, these two lifetimes are split into four separate exponential decays. As the principle method of lifetime analysis for TCSPC systems is nonlinear least squares curve fitting, this results in four distinct decay parameters in Eq. 3.1. As the number of photons required to adequately fit a curve rises with each added parameter, this results in a photon count requirement of millions. However, a typical FLIM-FRET measurement count rate is ~200-300 photons per second with a total count of ~100,000 photons over the course of 5-10 minutes. Gathering enough photons for adequate 4τ fitting would result in measurement times of hours, far beyond the viability of live cell microscopy. The data requirement for a worthwhile four lifetime fit is in fact so high that the B&H analysis software is limited to three lifetimes. In order to

overcome the data requirements imposed by the multi-exponential CFP fluorophore, we replaced it with a different label, teal fluorescent protein (TFP).

4.2. FLIM-FRET using TFP-YFP

Teal fluorescent protein (TFP) is a light blue fluorophore similar to CFP in terms of excitation and emission spectra, but displays a mono-exponential lifetime decay profile. In order to reduce the complexity of the nonlinear curve fit in the analysis stage, we have replaced prestin-CFP with a new construct prestin-TFP. This new construct was first transfected in HEKs without a complementing FRET acceptor, resulting in a measured lifetime of 2.38ns ± 33ps that was well fit by a single decay model (data not shown. In Figure 4.2, the prestin-TFP construct is compared against prestin-CFP as a FRET donor in both AP-FRET and FLIM-FRET measurements. TFP-YFP FLIM traces were fit with a bi-exponential decay model. The transfer efficiency is a remarkable 90.7% ±1.2%, much higher than CFP-YFP in either system; however, the standard deviation of the measurement is smaller than that of AP-FRET.

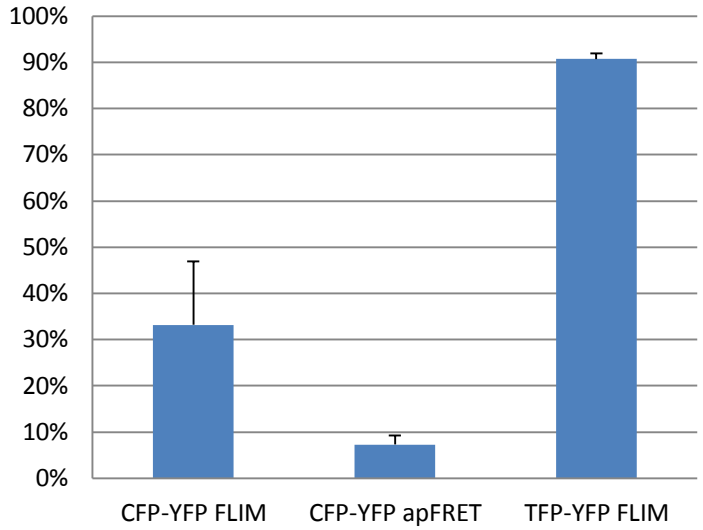

Figure 4.2 FRET efficiencies *E* of wildtype prestin in different systems. The CFP measurements are the same as those in Figure 4.1. FLIM imaged TFP-YFP *E*=90.7% with a standard deviation of 1.2%.

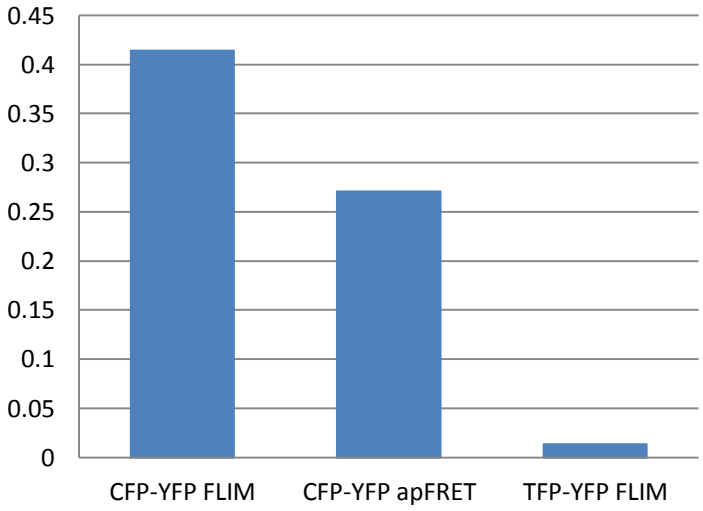

Figure 4.3. Relative standard deviation of FRET methods. RSDs for each FRET system are 0.41 for CFP-YFP FLIM-FRET, 0.27 for CFP-YFP AP-FRET, and 0.01 for TFP-YFP FLIM FRET.

In Figure 4.3 above, the standard deviations of the FRET measurements are restated in terms of relative standard deviation:

$$RSD = \frac{SD(X)}{AVG(X)} \tag{4.1}$$

The RSD of a measurement is comparable to the precision achieved in that measurement, with smaller RSD values indicating greater precision as the standard deviation of a measurement becomes smaller with respect to the absolute measurement. Clearly, the use of fluorescence lifetime based FRET detection alone is not enough to realize accuracy gains, as FLIM-FRET compares poorly with AP-FRET when using CFP-YFP as the fluorophore pair. TFP-YFP FLIM-FRET, on the other hand, has a reported efficiency of the so high that, under the usual $\kappa^2=2/3$ assumption for Equation 2.2, the TFP and YFP fluorophores would actually be collapsed upon each other. Utilizing a nominal R_0 value of 5.7nm for the TFP-YFP pair [], FRET efficiencies of 80% would imply that a distance between the chromophores of ~4nm; fluorescent proteins, including TFP and YFP, generally have a diameter of ~4nm. Though the randomly rotating dipoles assumption for κ was never actually applicable to prestin constructs as the fluorophores are anchored to the c-terminus and therefore unable to freely rotate, it is evident that dipole orientation cannot be assumed away.

4.3. Voltage Controlled Prestin Association

Making use of both TFP as a simple, reliable donor fluorophore and FLIM as high accuracy measurement technique, we proceed to investigate the response of prestin oligomers in response to transmembrane potentials. Using whole-cell patch clamp, HEKs cotransfected with prestin-TFP and prestin-YFP constructs were held at fixed voltages while FLIM-FRET measurements were conducted. Each cell is tested for prestin function by running an NLC trace. These cells are then held at either -80mV, -50mV, -25mV, 0mV, 25mV, 50mV, or 90mV for the duration of the experiment. A FLIM measurement is then begun as usual, but is terminated immediately if the patch integrity is lost during the course of the experiment. As was done previously, TFP fluorescence decay traces were fit to a bi-exponential decay model; fits with χ^2_r values greater than 1.2 were not included in the final data set. Figure 4.4 summarizes the results of these experiments and includes a two-state Boltzmann distribution fit. Table 1 lists the fitted parameters and associated standard deviations.

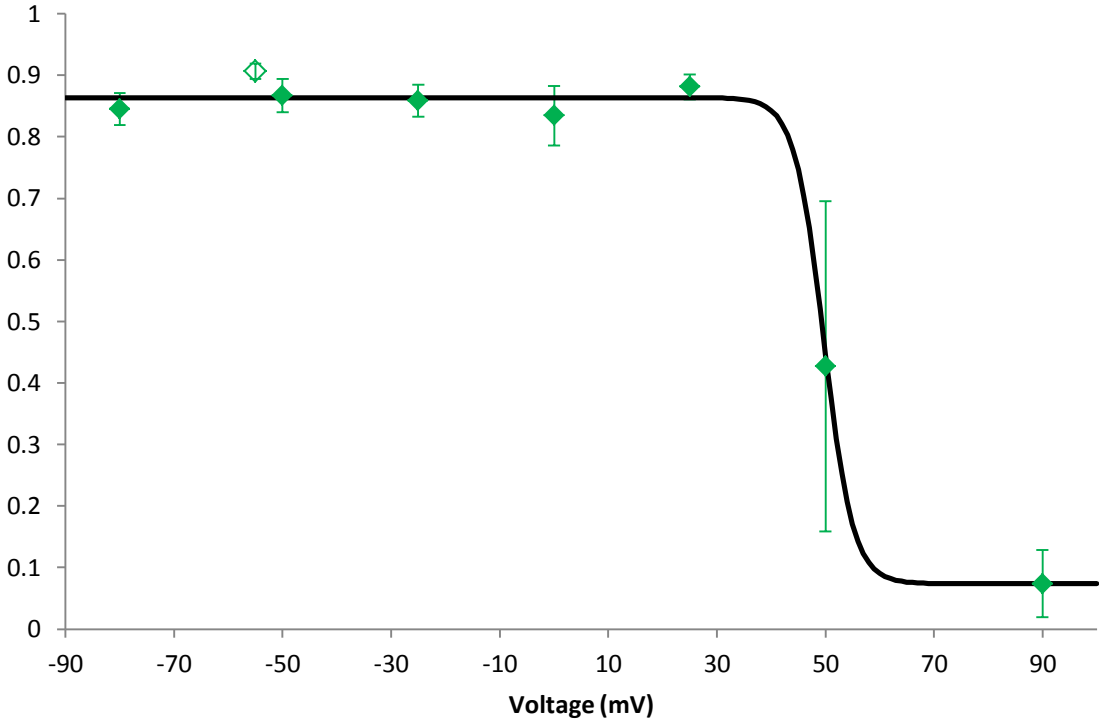

Figure 4.4 Voltage FRET in Prestin HEKs. Green: FRET efficiencies of prestin-TFP and prestin-YFP recorded by FLIM-FRET under voltage-clamp. Bars represent standard deviation. Black: Two-state Boltzmann distribution fit to FRET data. The closed diamond is the FRET efficiency of unpatched prestin HEKs.

Membrane Potential	τ1/ps	SD(τ1)	τ2/ps	SD(τ2)	α1	α2	SD(α)	$E=1-\tau_1/\tau_2$	SD(E)	n
-80mV	353	54	2280	76	19.5%	80.5%	4.8	84.5%	2.6%	5
-50mV	327	63	2373	66	24.7%	75.4%	7.8	86.7%	2.7%	6
-25mV	329	53	2343	63	26.9%	73.2%	7.9	85.9%	2.6%	6
0mV	382	108	2312	36	25.4%	74.6%	5.4	83.4%	4.8%	5
25mV	287	53	2408	74	19.3%	80.7%	6.6	88.1%	2.0%	6
50mV	1161	779	2405	253	30.8%	65.5%	20.2	42.7%	26.8%	6
90mV	2305	55	2493	109	66.2%	33.8%	3.2	7.4%	5.4%	3
At rest	215	31	2304	61	50.0%	50.0%	11.1	90.7%	1.2%	8
TFP Only	--	--	2385	33	100%	--	--	--	--	10

Table 1. Voltage controlled prestin FLIM-FRET in HEK cells. Each TFP lifetime trace is fit to a bi-exponential decay model, from which a FRET efficiency *E* is calculated. Fitted parameters are donor-acceptor lifetime (τ_1), donor lifetime (τ_2), normalized pre-exponential factors for each lifetime component (α). At rest cells are unpatched prestin HEKs. Lifetime data from unpatched HEKs transfected with prestin-TFP included for reference.

The FLIM-FRET data shows a clear voltage dependence in FRET efficiency. Transmembrane voltages from-90mV to 25mV result in high FRET efficiencies, while 90mV disrupts FRET activity. The 50mV data point has a very large standard deviation of 26.8%. The two-state Boltzmann distribution is easily fit to these results, and suggests an interpretation of the data where the high and low FRET efficiencies are the result of two distinct conformational states. At 50mV, the probability that a particular prestin molecule would be in either conformational state is 50%, leading to a population consisting of an equal mixture of both states. This population would have a distribution of lifetimes that could not be easily fit to a bi-exponential decay model, leading to a high margin of error in the measurement.

4.4. Discussion and Future Direction

Initial lifetime measurements used the conventional FRET pair of CFP-YFP, each attached to separate prestin constructs. Although FLIM-FRET reported higher raw FRET efficiency, the results of these initial studies were actually more imprecise than acceptor photobleach studies performed on the same construct (Figure 4.3). This was the result of poor curve fitting results due to low photon counts as well as the inherent complexity of using CFP, a bi-exponential decay donor that actually possesses four decay lifetimes when in a FRET system. In order to remedy these issues, TFP was selected as a replacement donor fluorescent protein in prestin constructs. As TFP is brighter than CFP and exhibits monoexponential decay, more

photons were collected and were fit to a less complex two lifetime decay model, leading to better results overall.

With a high precision FRET platform, a combination of robust instrumentation and fluorescent proteins, now developed and implemented, we have investigated the conformational changes in prestin-prestin conformational states. There is strong evidence for voltage dependent conformation in prestin-prestin oligomers that fits well to a theory of prestin as a two-state protein. However, the large changes in FLIM-FRET efficiency in this study may not be interpreted solely as distance changes. Disentangling the contributions of dipole orientation and distance is not possible with FLIM-FRET alone, and will require further study.

This thesis has laid the groundwork for the further investigation of the electromechanical action of prestin in the cellular membrane. This experimental platform can be used to study the action of prestin with greater precision than any other measurement to date.

References

1. Chittka, L. and A. Brockmann, *Perception space - The final frontier.* Plos Biology, 2005. **3**(4): p. 564-568.
2. Geisler, C.D., *From sound to synapse : physiology of the mammalian ear*. 1998, New York: Oxford University Press. xiv, 381 p.
3. Gold, T., *Hearing .2. The Physical Basis of the Action of the Cochlea.* Proceedings of the Royal Society B-Biological Sciences, 1948. **135**(881): p. 492-498.
4. Gray, H. and W.H. Lewis, *Anatomy of the human body*. 20th ed. 1918, Philadelphia and New York,: Lea & Febiger.
5. Bekesy, G.V., *Travelling Waves as Frequency Analysers in Cochlea.* Nature, 1970. **225**(5239): p. 1207-&.
6. Kandel, E.R., J.H. Schwartz, and T.M. Jessell, *Principles of neural science*. 4th ed. 2000, New York: McGraw-Hill, Health Professions Division. xli, 1414 p.
7. Dallos, P., A.N. Popper, and R.R. Fay, *The cochlea*. Springer handbook of auditory research. 1996, New York: Springer. xii, 551 p.
8. Ashmore, J.F., *A fast motile response in guinea-pig outer hair cells: the cellular basis of the cochlear amplifier.* J Physiol, 1987. **388**: p. 323-47.
9. Kachar, B., et al., *Electrokinetic shape changes of cochlear outer hair cells.* Nature, 1986. **322**(6077): p. 365-8.
10. Brownell, W.E., et al., *Evoked mechanical responses of isolated cochlear outer hair cells.* Science, 1985. **227**(4683): p. 194-6.
11. Santos-Sacchi, J., *Reversible inhibition of voltage-dependent outer hair cell motility and capacitance.* J Neurosci, 1991. **11**(10): p. 3096-110.
12. Zheng, J., et al., *Prestin is the motor protein of cochlear outer hair cells.* Nature, 2000. **405**(6783): p. 149-55.
13. Dallos, P., et al., *Prestin-based outer hair cell motility is necessary for mammalian cochlear amplification.* Neuron, 2008. **58**(3): p. 333-9.
14. Liberman, M.C., et al., *Prestin is required for electromotility of the outer hair cell and for the cochlear amplifier.* Nature, 2002. **419**(6904): p. 300-4.
15. Deak, L., et al., *Effects of cyclic nucleotides on the function of prestin.* J Physiol, 2005. **563**(Pt 2): p. 483-96.
16. Dallos, P. and B. Fakler, *Prestin, a new type of motor protein.* Nat Rev Mol Cell Biol, 2002. **3**(2): p. 104-11.
17. Yu, N., M.L. Zhu, and H.B. Zhao, *Prestin is expressed on the whole outer hair cell basolateral surface.* Brain Res, 2006. **1095**(1): p. 51-8.
18. McGuire, R.M., et al., *Selective cell-surface labeling of the molecular motor protein prestin.* Biochem Biophys Res Commun, 2011. **410**(1): p. 134-9.
19. Mount, D.B. and M.F. Romero, *The SLC26 gene family of multifunctional anion exchangers.* Pflugers Arch, 2004. **447**(5): p. 710-21.
20. Mistrik, P., et al., *Mammalian prestin is a weak Cl-/HCO3- electrogenic antiporter.* J Physiol, 2012. **590**(Pt 22): p. 5597-610.

21. Muallem, D. and J. Ashmore, *An anion antiporter model of prestin, the outer hair cell motor protein.* Biophys J, 2006. **90**(11): p. 4035-45.
22. Tan, X., et al., *From zebrafish to mammal: functional evolution of prestin, the motor protein of cochlear outer hair cells.* J Neurophysiol, 2011. **105**(1): p. 36-44.
23. Weber, T., et al., *Expression of prestin-homologous solute carrier (SLC26) in auditory organs of nonmammalian vertebrates and insects.* Proc Natl Acad Sci U S A, 2003. **100**(13): p. 7690-5.
24. Oliver, D., et al., *Intracellular anions as the voltage sensor of prestin, the outer hair cell motor protein.* Science, 2001. **292**(5525): p. 2340-3.
25. Gulley, R.L. and T.S. Reese, *Regional specialization of the hair cell plasmalemma in the organ of corti.* Anat Rec, 1977. **189**(1): p. 109-23.
26. Greeson, J.N., et al., *Assessment of prestin self-association using fluorescence resonance energy transfer.* Brain Res, 2006. **1091**(1): p. 140-50.
27. Santos-Sacchi, J., *Harmonics of outer hair cell motility.* Biophys J, 1993. **65**(5): p. 2217-27.
28. Dallos, P., R. Hallworth, and B.N. Evans, *Theory of electrically driven shape changes of cochlear outer hair cells.* J Neurophysiol, 1993. **70**(1): p. 299-323.
29. Raphael, R.M., A.S. Popel, and W.E. Brownell, *A membrane bending model of outer hair cell electromotility.* Biophys J, 2000. **78**(6): p. 2844-62.
30. Forster, T., **Zwischenmolekulare Energiewanderung Und Fluoreszenz.* Annalen Der Physik, 1948. **2**(1-2): p. 55-75.
31. Lakowicz, J.R., *Principles of fluorescence spectroscopy*. 2nd ed. 1999, New York: Kluwer Academic/Plenum. xxiii, 698 p.
32. Truong, K. and M. Ikura, *The use of FRET imaging microscopy to detect protein-protein interactions and protein conformational changes in vivo.* Curr Opin Struct Biol, 2001. **11**(5): p. 573-8.
33. Ormo, M., et al., *Crystal structure of the Aequorea victoria green fluorescent protein.* Science, 1996. **273**(5280): p. 1392-5.
34. Jares-Erijman, E.A. and T.M. Jovin, *FRET imaging.* Nat Biotechnol, 2003. **21**(11): p. 1387-95.
35. Lleres, D., et al., *Quantitative analysis of chromatin compaction in living cells using FLIM-FRET.* J Cell Biol, 2009. **187**(4): p. 481-96.
36. Albertazzi, L., et al., *Quantitative FRET analysis with the EGFP-mCherry fluorescent protein pair.* Photochem Photobiol, 2009. **85**(1): p. 287-97.
37. Becker, W., *The bh TCSPC Handbook*. 3rd ed. 2008, Berlin, Germany. xi, 466p.
38. Kaiser, W. and C.G.B. Garrett, *Two-Photon Excitation in CaF_{2}: Eu^{2+}.* Physical Review Letters, 1961. **7**(6): p. 229-231.
39. Franken, P.A., et al., *Generation of Optical Harmonics.* Physical Review Letters, 1961. **7**(4): p. 118-119.
40. Zoumi, A., A. Yeh, and B.J. Tromberg, *Imaging cells and extracellular matrix in vivo by using second-harmonic generation and two-photon excited fluorescence.* Proceedings of the National Academy of Sciences, 2002. **99**(17): p. 11014-11019.

41. Hodgkin, A.L. and A.F. Huxley, *Propagation of electrical signals along giant nerve fibers.* Proc R Soc Lond B Biol Sci, 1952. **140**(899): p. 177-83.
42. Mergler, S. *Conventional patch-clamp technique*. 2010 Aug. 2010 [cited 2012 Jan. 4]; Available from: http://patch-clamp.info/techniques/techniques.htm.
43. Neher, E. and B. Sakmann, *Single-channel currents recorded from membrane of denervated frog muscle fibres.* Nature, 1976. **260**(5554): p. 799-802.
44. Lakowicz, J.R. and C.D. Geddes, *Topics in fluorescence spectroscopy*. 1991, New York: Plenum Press. v. <1-10>.